Effects of Ti, Ni, and Dual Ti/Ni Plasma Immersion Ion Implantation on the Corrosion and Wear Properties of Magnesium Alloy

Jun Dai [1,2,*], **Zheng Liu** [3,*], **Banglong Yu** [1], **Qingdong Ruan** [2] **and Paul K. Chu** [2]

1   School of Automotive Engineering, Changshu Institute of Technology, Changshu 215500, China; yubanglong@163.com
2   Department of Physics, Department of Materials Science and Engineering and Department of Biomedical Engineering, City University of Hong Kong, Kowloon 999077, China; qingruan@cityu.edu.hk (Q.R.); paul.chu@cityu.edu.hk (P.K.C.)
3   School of Mechanical Engineering, Guilin University of Aerospace Technology, Guilin 541004, China
*   Correspondence: jdaijs@163.com (J.D.); liuzheng@guat.edu.cn (Z.L.)

Abstract: Ti, Ni, and Ti/Ni plasma immersion ion implantation is carried out on the AM60 magnesium alloy with a 6×10^{16} ions/cm^2 fluence and energy of 35 keV. The corrosion and wear properties of the ion-implanted samples are determined systematically by X-ray photoelectron spectroscopy, X-ray diffraction, scanning electron microscopy, electrochemical methods and wear tests. A Ni-rich layer composed of α-Mg, Ni$_2$O$_3$, and NiTi$_2$ is formed on the surface after dual Ti/Ni ion implantation, and the ion implantation range is approximately 300 nm. The corrosion resistance of the Ni- and Ti/Ni-implanted AM60 samples is significantly reduced in the 3.5% NaCl solution. However, NiTi$_2$ does not adhere well to the grinding ring during the wear test due to the bonding properties, and the sample implanted with both Ti and Ni shows the best wear resistance.

Keywords: magnesium alloy; plasma ion implantation; Ti/Ni coatings; corrosion resistance; wear resistance

1. Introduction

Magnesium alloys are widely used in many fields because of their light weight, good damping capacity, and recycling potential [1–3]. Unfortunately, the corrosion resistance of magnesium alloys in many engineering applications is insufficient [4,5] and methods such as micro-arc oxidation [6,7], laser cladding [8,9], plasma electrolytic oxidation [10,11] and ion implantation [12–15] have been proposed to improve the corrosion properties. For example, Zn [16,17], Zr [18], Nd [19], C$_2$H$_2$ [20] and Si [21] ion implantations have been conducted on Mg alloys to improve the surface properties [17,22].

Some duplex coatings such as Ti/N [23,24], Al/N [25], Zr/N [26] and Cr/O [27] have also been investigated. AZ31 Mg Alloy samples with N and Ti duplex ion implantation possess a significantly improved corrosion resistance. Dual Zr/N plasma ion implantation forms a 53 nm thick Zr rich layer and a 66 nm thick N rich layer on the WE43 Mg alloy. The corrosion resistance of the Mg alloy sample is improved following dual ion implantation.

It is difficult for the composition of single-ion implantation to meet the various requirements in harsh environments. There are few studies on the interaction between ions after duplex ion implantation. Metal ions and non-metal ions are usually used together to improve the properties of Mg alloys. In spite of recent advances, dual metal ion implantation on AM60 magnesium alloy has seldom been performed with successful outcomes.

In this work, AM60 magnesium alloy is implanted with Ti, Ni, as well Ti/Ni. The corrosion and wear properties of the various samples were studied in detail and the mechanism was investigated with the aid of first-principles calculation.

2. Experimental Details and Theoretical Calculation

AM60 magnesium alloy plates with dimensions of 15 mm × 15 mm × 2 mm were ground with SiC paper up to 2000# and ultrasonically cleaned in alcohol for 5 min. Plasma immersion ion implantation was carried out on the PI-80A plasma immersion ion implanter in City University of Hong Kong's Plasma Laboratory. The base pressure in the vacuum chamber was 2×10^{-3} Pa and Ti/Ni ion implantation was performed at an accelerating voltage of 35 keV with a fluence of 6×10^{16} ions/cm^2. Sample "Ti" was implanted with Ti only, sample "Ni" with Ni only, and sample "TiNi" with Ti and then Ni. To compare results, the properties of the un-implanted base metal AM60 (BM) were determined under the same conditions.

To determine the elemental depth profile and chemical states of the implanted samples, an X-ray photoelectron spectroscopy (XPS, PHI-5000 Versaprobe, Kanagawa, Japan) was completed with Al K_α irradiation at a sputtering rate of approximately 10 nm/min. The sputtering rate was estimated to be approximately 10 nm/min based on the analysis of a standard SiO$_2$ film under the same conditions. The structure was analyzed by X-ray diffraction on the D2 Phaser X-ray diffractometer (XRD) (BRUKER, Karlsruhe, Germany) with Cu K_α radiation. Immersion corrosion tests were carried out to evaluate the corrosion properties in 3.5% NaCl and after immersion for 24 h, the samples were observed by scanning electron microscopy (SEM, ZEISS SIGMA500, Dresden, Germany) and analyzed by XRD.

The wear resistance performance was tested by a ball-on-disc wear tester (CETR UMT-2, CA, USA) at a relative humidity of 35% and temperature of 25 °C using a Si$_3$N$_4$ ball with a radius of 1.5 mm. The sliding distance and rotation rate were 3 mm and 200 r/min, respectively. The wear depths were measured by a profilometer (LK120H, JHJM, Xi'an, China) to evaluate the wear resistance after 30 min.

First-principles calculation was performed based on the density-functional theory and supersoft pseudopotential method. The crystal structure of NiTi$_2$ was constructed to calculate the electronic structure [28]. The CASTEP module in Materials Studio software was implemented to perform generalized gradient approximation (GGA) on the NiTi$_2$ crystal structure and the equation was self-consistently solved by Kohn–Sham. Before the calculation, the unit cell constant of NiTi$_2$ and each atomic lattice were fully relaxed until the unit cell energy converged to a fixed value. The results were not related to spin effects.

3. Results and Discussion

Figure 1 depicts the XPS depth profile of the Ti/Ni ion-implanted AM60 alloy. A Ni-rich layer forms on the surface after Ti/Ni ion implantation and the ion implantation range is approximately 300 nm. The Ni atom concentration decreases with the increase in depth. The Ti atom concentration first increases and then decreases with depth. When the depth is 100 nm, the Ti concentration is 25%. A surface oxide layer with a thickness of 150 nm is present on the surface due to air exposure. The high-resolution XPS spectra of O, Mg, Ti, and Ni acquired after various sputtering times are shown in Figure 2. In Figure 2a, the O peak intensity decreases as the sputtering time increases, and O is observed at the sputtering times of 0 min and 15 min. The Mg intensity increases gradually with sputtering time as shown in Figure 2b. In Figure 2c, the intensity of Ti increases at 15 min and then decreases at 30 min, and the largest concentration of Ti is observed in the middle of the layer. The intensity of Ni decreases with sputtering time as displayed in Figure 2d.
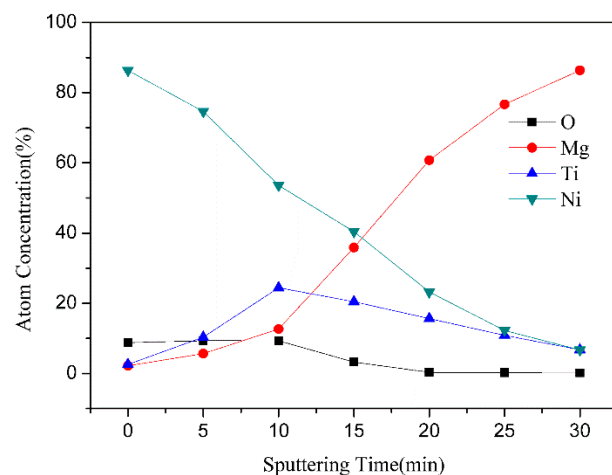
Figure 1. XPS elemental depth profiles acquired from the AM60 alloy after Ti/Ni ion implantation.
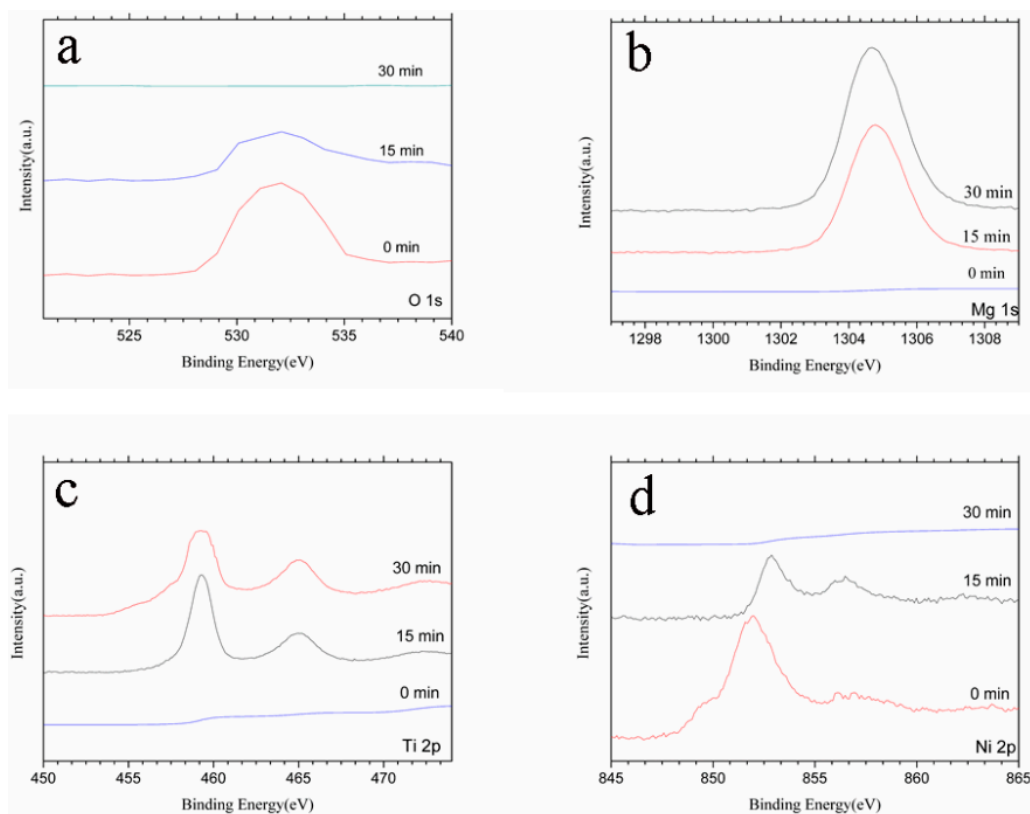
Figure 2. High-resolution XPS spectra of the treated AM60 alloy after various sputtering times: (**a**) O 1s, (**b**) Mg 1s, (**c**) Ti 2p, and (**d**) Ni 2p.

Figure 3 shows the XRD patterns of different samples. There are α-Mg and TiO_2 on the surface of sample Ti and some Ni_2O_3 and $NiTi_2$ on the surface of sample TiNi. Some oxides such as TiO_2 and Ni_2O_3 are produced after ion implantation and exposure to air. Some $NiTi_2$ compounds are produced during dual ion implantation. It can be speculated that there is a reaction between Ti and Ni ions in the process of ion implantation.
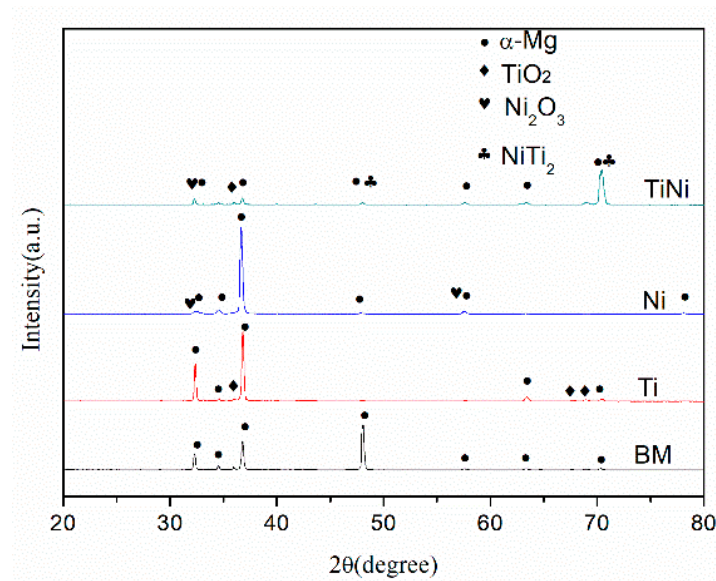
Figure 3. XRD patterns of different samples.

The morphology of the samples after immersion in 3.5% NaCl is displayed in Figure 4. There is little corrosion product on the surface of sample Ti as shown in Figure 4b, but samples Ni and TiNi were consumed by corrosion. Large amounts of corrosion products are observed on the surfaces of samples Ni and TiNi in Figure 4c,d. According to the Darken–Gurry principle of alloy design, Ti and Ni are situated all around the Darken–Gurry ellipse with Mg as the center as shown in Figure 5. Based on Pauling theory, the difference in the electronegativity between two elements indicates the strength of chemical affinity [29]. Electronegativity is the scale of the ability of an element's atom to attract electrons in a compound. The greater the electronegativity of an element, the stronger the ability of its atom to attract electrons in the compound. The electronegativity values of Ni, Mg and Ti are 1.92, 1.31 and 1.54, respectively. The electronegativity difference between Ti and Mg (0.23) is less than that between Ni and Mg (0.61). Hence, Ni and Mg tend to be coupled, giving rise to electrode reactions and electrochemical corrosion. The main reaction is:
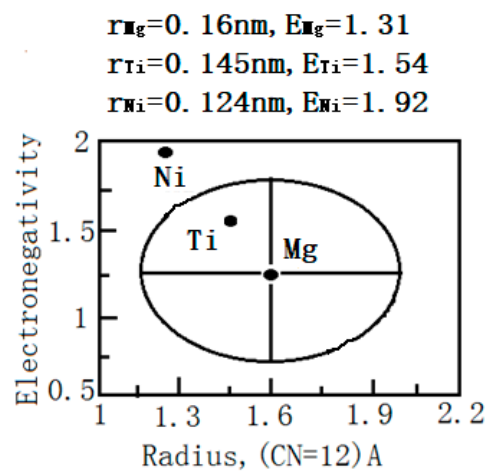
$$Mg + Ni_2O_3 + 3H_2O > Mg(OH)_2 + 2Ni(OH)_2$$
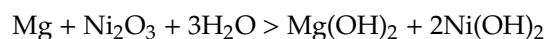
According to XRD results acquired from the corrosion products shown in Figure 4d-1, the main products are $Mg(OH)_2$ and $2Ni(OH)_2$.
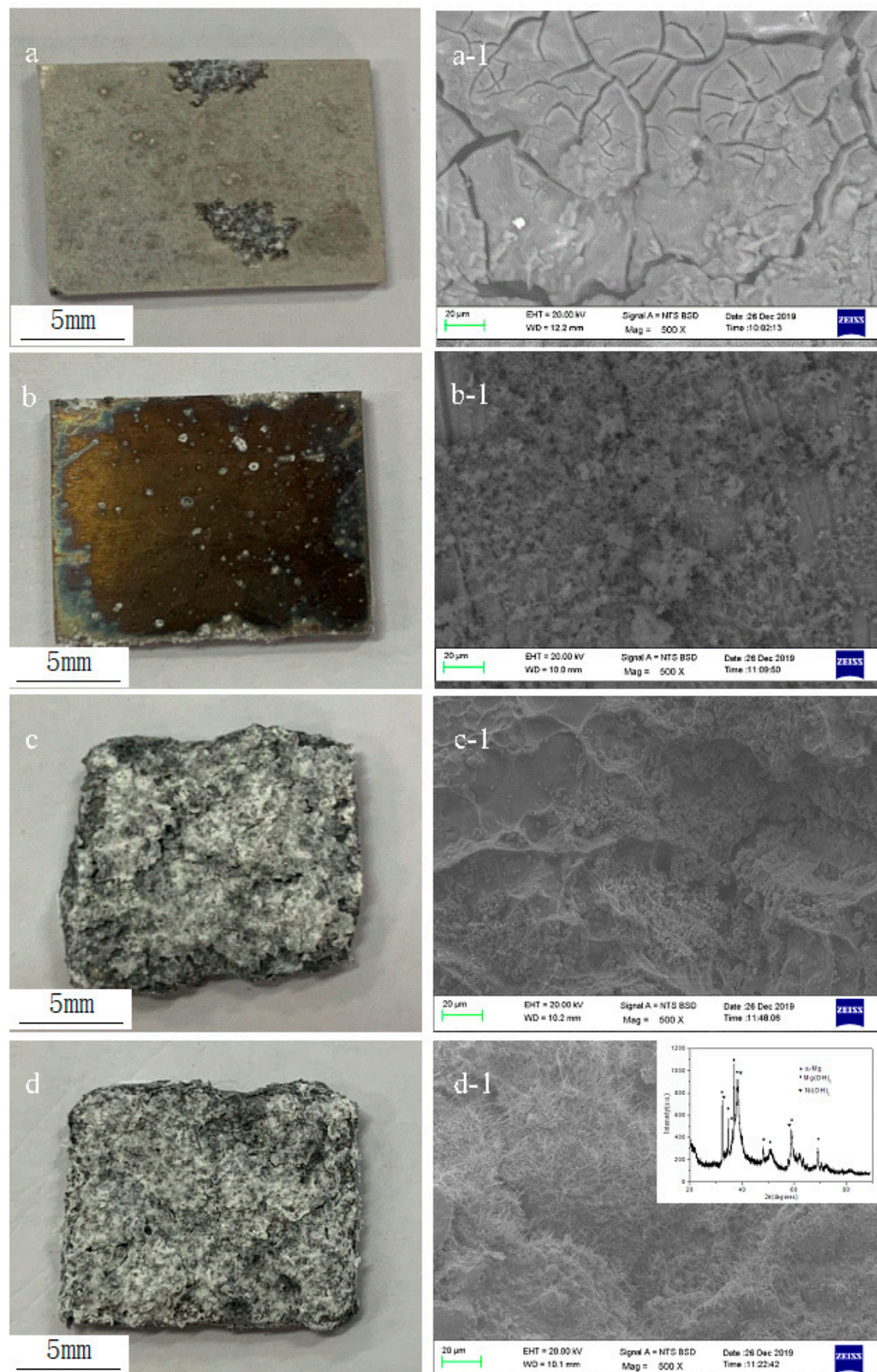
Figure 4. Morphology of the corroded samples: (**a**) BM, (**b**) Ti, (**c**) Ni, (**d**) TiNi, (i-1) High-magnification SEM pictures, (*I* = a, b, c, and d).

Figure 5. Position of Ti and Ni in the Darken–Gurry ellipse of Mg and electronegativity.

Figure 6 shows the wear depths of different samples. The depth of sample BM is 100.03 μm which is larger than those of other samples. The depths of sample Ti and sample Ni are 52.63 μm and 40.56 μm, respectively. In comparison, sample TiNi exhibits the smallest wear depth (20.26 μm) and the best wear resistance. The oxide layer on the surface produces microcracks which expand gradually leading to the oxide film eventually cracking and peeling off to form wear debris. The calculation of the worn volume is shown as follows:

$$w_d = 2\pi r A/pl$$

where w_d is worn volume (mm^3/mN), r is wear radius (mm), A is profile area of wear mark (mm^2), p is load (N), l is wear route (m), $l = 2\pi rvt$, v is rotation rate (r/min), and t is wear time (min).

The worn volume results of different samples are shown in Table 1. It can be seen that the worn volume of the BM sample is much larger than the ion implantation samples. The sample TiNi has the smallest worn volume.
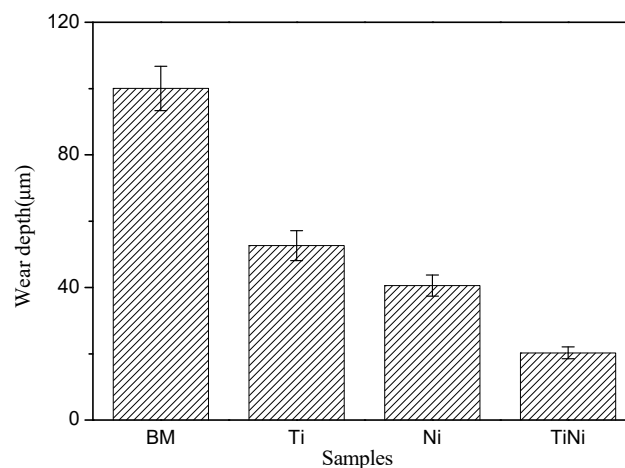
**Figure 6.** Wear depths of different samples.

Table 1. Worn volume results of different samples.

Samples	Width (mm)	Depth (μm)	Worn Volume (10^{-6} mm^3·m^{-1}·N^{-1})
BM	0.62	100.03	2583
Ti	0.54	52.63	702
Ni	0.44	40.56	440
TiNi	0.31	20.26	155

In order to provide helpful guidance in understanding the wear properties of samples and finding the action of NiTi$_2$ after ion implantation, a first-principles calculation is performed based on the density-functional theory and the supersoft pseudopotential method as aforementioned. NiTi$_2$ has a complex cubic structure. According to Find It, the NiTi$_2$ space group is Fd-3m (parameter code 227) and $a = b = c = 11.3193$ Å as displayed in Table 2. Accordingly, a unit cell model is established as shown in Figure 7a, and the electron density map is shown in Figure 7b. Figure 7c shows that d electrons cross the Fermi level in the density of states (DOS) of NiTi$_2$. The electron energy contributing to bonding is mainly concentrated in the range between −40 eV and −30 eV, and the main source is the valence electron contribution of Ti(p), Ti(d), Ni(d). As shown in Figure 7, there are metallic bonds in NiTi$_2$ compounds. It has a high hardness and is difficult to deform under the action of contact stress during the wear test. It can be indicated that NiTi$_2$ does not adhere well to the grinding ring due to the bonding property. Formation of NiTi$_2$ in the dual ion-implanted layer prevents the formation and propagation of microcracks on the surface, and consequently, the wear properties of the sample TiNi are significantly improved after Ti/Ni ion implantation [30].

Table 2. Lattice parameters of NiTi$_2$.

Crystal	Space Group	Lattice Parameters			Elements	Atomic Coordinates		
		a	*b*	*c*		*X*	*Y*	*Z*
NiTi$_2$	227	11.3193	11.3193	11.3193	Ni (I)	0.912	0.912	0.912
					Ti (II)	0.311	0	0
					Ti (II)	0.125	0.125	0.125
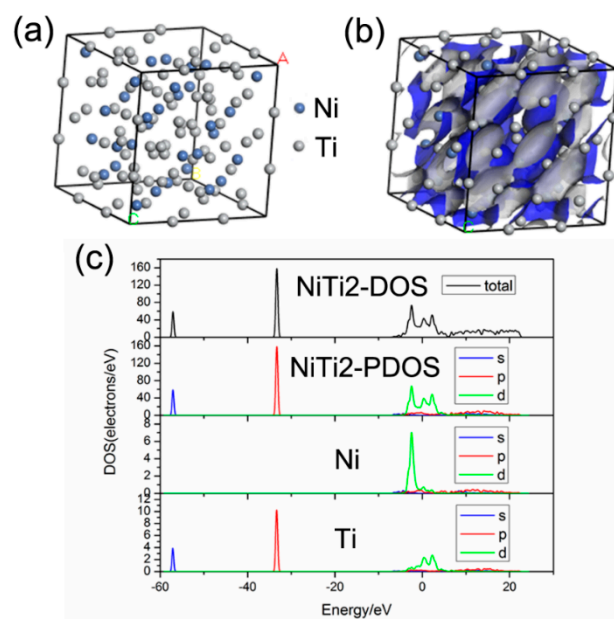
Figure 7. First-principles study of NiTi$_2$: (**a**) Unit cell model, (**b**) Electron density map, and (**c**) State density maps.

4. Conclusions

A Ni-rich layer forms on the surface after dual Ti/Ni ion implantation, and the ion implantation range is approximately 300 nm. There are α-Mg, Ni_2O_3 and $NiTi_2$ in the near-surface after Ti/Ni ion implantation. The corrosion resistance of the Ni and Ti/Ni samples decreases in 3.5% NaCl. The wear depth measured from the Ti/Ni sample is 20.26 μm. $NiTi_2$ does not adhere well to the grinding ring due to the bonding property during the wear test. Comparing the three samples, dual Ti/Ni ion implantation into AM60 alloy shows the best wear resistance.

References

1.　Shaha, S.K.; Dayani, S.B.; Xue, Y.N. Improving corrosion and corrosion-fatigue resistance of AZ31B cast mg alloy using combined cold spray and top coatings. *Coatings* **2018**, *8*, 443. [CrossRef]

2.　Polmear, I.J. Magnesium alloys and applications. *Mater. Sci. Technol.* **1994**, *10*, 1–16. [CrossRef]

3.　Mukai, T.; Yamanoi, M.; Watanabe, H.; Higashi, K. Ductility enhancement in AZ31 magnesium alloy by controlling its grain structure. *Scr. Mater.* **2001**, *45*, 89–94. [CrossRef]

4.　Rahmati, M.; Raeissi, K.; Toroghinejad, M.R. Effect of pulse current mode on microstructure, composition and corrosion performance of the coatings produced by plasma electrolytic oxidation on AZ31 Mg alloy. *Coatings* **2019**, *9*, 688. [CrossRef]

5.　Song, D.; Li, C.; Liang, N.N.; Yang, F.L.; Jiang, J.H.; Sun, J.P.; Wu, G.S.; Ma, A.; Ma, X.L. Simultaneously improving corrosion resistance and mechanical properties of a magnesium alloy via equal-channel angular pressing and post water annealing. *Mater. Des.* **2019**, *166*, 107621. [CrossRef]

6.　Jian, S.Y.; Ho, M.L.; Shih, B.C. Evaluation of the corrosion resistance and cytocompatibility of a bioactive micro-arc oxidation coating on AZ31 Mg alloy. *Coatings* **2019**, *9*, 396. [CrossRef]

7.　Cui, X.J.; Lin, X.Z.; Liu, C.H.; Yang, R.S.; Zheng, X.W.; Gong, M. Fabrication and corrosion resistance of a hydrophobic micro-arc oxidation coating on AZ31 Mg alloy. *Corros. Sci.* **2015**, *90*, 402–412. [CrossRef]

8.　Ignat, S.; Sallamand, P.; Grevey, D.; Lambertin, M. Magnesium alloys laser (Nd: YAG) cladding and alloying with side injection of aluminium powder. *Appl. Surf. Sci.* **2004**, *225*, 124–134. [CrossRef]

9.　Liu, J.L.; Yu, H.J.; Chen, C.Z.; Weng, F.; Dai, J.J. Research and development status of laser cladding on magnesium alloys: A review. *Opt. Lasers. Eng.* **2017**, *93*, 195–210. [CrossRef]

10.　Luca, P.; Leonardo, B.C.; Rachele, B.; Alessio, G.S.; Katya, B.; Marjorie, O.; Dabalà, M. Corrosion and mechanical properties of plasma electrolytic oxidation-coated AZ80 magnesium alloy. *Mater. Corros.* **2019**, *70*, 2103–2112.

11.　Luca, P.; Michele, R.; Alessandro, M.; Katya, B.; Manuele, D. Plasma Electrolytic Oxidation (PEO) as pre-treatment for sol-gel coating on aluminum and magnesium alloys. *Surf. Coat. Technol.* **2019**, *366*, 114–123.

12.　Wu, G.S.; Jamesh, M.I.; Chu, P.K. Surface design of biodegradable magnesium alloys—A review. *Surf. Coat. Technol.* **2013**, *233*, 2–12. [CrossRef]

13.　Jamesh, M.I.; Wu, G.S.; Zhao, Y.; McKenzie, D.R.; Bilek, M.M.; Chu, P.K. Electrochemical corrosion behavior of biodegradable Mg-Y-RE and Mg-Zn-Zr alloys in Ringer's solution and simulated body fluid. *Corros. Sci.* **2015**, *91*, 160–184. [CrossRef]

14.　Feliu, S.; Maffiotte, C.; Samaniego, A.; Galvan, J.C.; Barranco, V. Effect of the chemistry and structure of the native oxide surface film on the corrosion properties of commercial AZ31 and AZ61 alloys. *Appl. Surf. Sci.* **2011**, *257*, 8558–8568. [CrossRef]

15. Zheng, Y.; Zhang, L.B.; Bi, Y.Z. Corrosion behavior of Fe/Zr composite coating on ZK60 Mg alloy by Ion implantation and deposition. *Coatings* **2018**, *8*, 261. [CrossRef]

16. Liu, J.; Zheng, Y.; Bi, Y.; Li, Y.; Zheng, Y.F. Improved cytocompatibility of Mg-1Ca alloy modified by Zn ion implantation and deposition. *Mater. Lett.* **2017**, *205*, 87–89. [CrossRef]

17. Wan, Y.Z.; Xiong, G.Y.; Luo, H.L.; He, F.; Huang, Y.; Wang, Y.L. Influence of zinc ion implantation on surface nanomechanical performance and corrosion resistance of biomedical magnesium–calcium alloys. *Appl. Surf. Sci.* **2008**, *254*, 5514–5516. [CrossRef]

18. Ba, Z.X.; Jia, Y.Q.; Dong, Q.S.; Li, Z.Z.; Kuang, J. Effects of Zr Ion implantation on surface mechanical properties and corrosion resistance of pure magnesium. *J. Mater. Eng. Perform.* **2019**, *28*, 2543–2551. [CrossRef]

19. Jin, W.H.; Wu, G.S.; Feng, H.Q.; Wang, W.H.; Zhang, X.M.; Chu, P.K. Improvement of corrosion resistance and biocompatibility of rare-earth WE43 magnesium alloy by neodymium self-ion implantation. *Corros. Sci.* **2015**, *94*, 142–155. [CrossRef]

20. Li, Z.C.; Shang, Z.Z.; Wei, X.; Zhao, Q. Corrosion resistance and cytotoxicity of AZ31 magnesium alloy with N+ ion implantation. *Mater. Technol.* **2019**, *34*, 730–736. [CrossRef]

21. Jamesh, M.I.; Wu, G.S.; Zhao, Y.; Chu, P.K. Effects of silicon plasma ion implantation on electrochemical corrosion behavior of biodegradable Mg–Y–RE Alloy. *Corros. Sci.* **2013**, *69*, 158–163. [CrossRef]

22. Husak, Y.; Solodovnyk, O.; Yanovska, A. Degradation and in vivo response of hydroxyapatite-coated Mg alloy. *Coatings* **2018**, *8*, 375. [CrossRef]

23. Liu, H.X.; Xu, Q.; Jiang, Y.H.; Wang, C.Q.; Zhang, X.W. Corrosion resistance and mechanical property of AZ31 magnesium alloy by N/Ti duplex ion implantation. *Surf. Coat. Technol.* **2013**, *228*, S538–S543. [CrossRef]

24. Wu, G.S.; Ding, K.J.; Zeng, X.Q.; Wang, X.M.; Yao, S.S. Improving corrosion resistance of titanium-coated magnesium alloy by modifying surface characteristics of magnesium alloy prior to titanium coating deposition. *Scr. Mater.* **2009**, *61*, 269–272. [CrossRef]

25. Xie, Z.W.; Chen, Q.; Chen, T.; Gao, X.; Yu, X.G.; Song, H.; Feng, Y.J. Microstructure and properties of nitrogen ion implantation/AlN/CrAlN/MoS2-phenolic resin duplex coatings on magnesium alloys. *Mater. Chem. Phys.* **2015**, *160*, 212–220. [CrossRef]

26. Jamesh, M.I.; Wu, G.S.; Zhao, Y.; Jin, W.H.; McKenzie, D.R.; Bilek, M.M.; Chu, P.K. Effects of zirconium and nitrogen plasma immersion ion implantation on the electrochemical corrosion behavior of Mg–Y–RE alloy in simulated body fluid and cell culture medium. *Corros. Sci.* **2014**, *86*, 239–251. [CrossRef]

27. Xu, R.Z.; Wu, G.S.; Yang, X.B.; Zhang, X.M.; Wu, Z.W.; Sun, G.Y.; Li, G.Y.; Chu, P.K. Corrosion behavior of chromium and oxygen plasma-modified magnesium in sulfate solution and simulated body fluid. *Appl. Surf. Sci.* **2012**, *258*, 8273–8278. [CrossRef]

28. Zhang, Y.; Guo, D.; Geng, H. Characterization of M-class genome segments of Muscovy duck reovirus S14. *Virus Res.* **2007**, *125*, 42–53. [CrossRef]

29. Zhang, B.W.; Liao, S.Z. Progress on the theories of solid solubility of alloy. *Shanghai Met.* **1999**, *21*, 3–9. (In Chinese)

30. Liu, Y.F.; Zhao, H.Y.; Wang, H.M.; Liu, G.P. Microstructure and wear resistance of laser clad Ti$_5$Si$_3$/(NiTi$_2$ + β + Ti$_5$Si$_3$) composite coating. *Mater. Sci. Technol.* **2002**, *338*, 126–132.